they were transparent and highly flexible, and showed a glassy fracture surface. The X-ray diffraction pattern of crushed fibre material (Fig. 2a) confirmed that it was glassy. This result is consistent with the report by Massiot *et al.*[6] that glassy YAG can be formed from the undercooled liquid. A photograph of several glass fibres is shown in Fig. 2b.

The initial experiments were performed on mixtures of the approximate $Y_3Al_5O_{12}$ (YAG) composition prepared from pure Al_2O_3 and Y_2O_3 powders. Some of the specimens readily formed long fibres whereas others did not, even though the melts were undercooled into the fibre-pulling temperature regime. In some cases only very short fibres of <1 mm in length were formed at the end of the stinger.

Later experiments showed that the variations in the fibre-pulling behaviour resulted from small differences in the compositions of the synthetic specimens. Fibres were rarely obtained if the melt was formed from stoichiometric single-crystal YAG, but long fibres were reproducibly pulled from compositions with an excess of 1 mol% Al_2O_3. Fibres were readily obtained from molten YAG compositions containing 1 mol Nd_2O_3 substituted for Y_2O_3. However, if Er_2O_3 was substituted for Y_2O_3 the behaviour was similar to that of stoichiometric YAG and fibres were rarely obtained. Addition of an excess of 1 mol% Al_2O_3 to the Er-containing material resulted in reproducible pulling of long glass fibres.

The initial sections of the fibres contained small nodules with smoothly varying diameters up to about four times the nominal fibre diameter and lengths that were a few times the nodule diameter. The central region of the long glass fibres was of uniform diameter, typically in the range 5–30 μm. The terminal sections of the fibres showed occasional nodular defects that were smaller, and appeared more abruptly than those in the initial section.

A further difference between the pure YAG and doped compositions was found in cooling experiments in which fibre-pulling was not conducted. Pure YAG compositions, and those with Er_2O_3 substituted for Y_2O_3 always crystallized when cooled below 1,400 K, but the compositions with excess Al_2O_3 or Nd_2O_3 substituted for Y_2O_3 formed a glass. In addition, the crystallization behaviour of pure YAG was sensitive to preheating conditions, such that either crystalline YAG or a mixture of $YAlO_3$ and Al_2O_3 could be formed.

In Fig. 3 we show data on the viscosity of molten YAG, as a semi-log plot of viscosity versus the ratio of the glass-transition temperature to the absolute temperature. The range of viscosities shown for fibre-pulling was taken to be that typical for glass-fibre manufacture, that is, $10^{1.5}$ to $10^{2.5}$ Pa s (ref. 9). This is the viscosity of the bulk liquid whose temperature was measured, and we recognize that further cooling of the liquid—and a further increase in viscosity—occurs in the meniscus leading to the fibres that form. This result is obtained for all of the compositions investigated. The sources of other data shown in Fig. 3 are given in the figure legend.

The lines in Fig. 3 confirm that molten YAG is a fragile glass-former. The viscosity versus T_g/T behaviour is similar to that of o-terphenyl, which is known to be an extremely fragile liquid[10]. We remark that, unlike many other glasses, both the present results and McMillan's measurement show that the value of T_g is well below two-thirds of the melting point of crystalline YAG.

There are at least two phenomena that may affect the fibre-pulling behaviour observed for pure YAG and doped compositions. The first is the greater sensitivity of undercooling behaviour in general for the pure composition. It is well known that YAG crystal growth can encounter difficulties due to crystallization of other phases[11,12]. Evidently, undercooled pure YAG melts are sensitive to small compositional or other differences associated with preheating, and this sensitivity may also influence the glass-fibre-pulling process.

The second phenomenon that may affect fibre-pulling was reported by Aasland and McMillan[13]. They found that a mixture of two glasses forms on rapid cooling of Al_2O_3–Y_2O_3 melts contain-ing 24–32 mol% Y_2O_3. The difficulty in making pure YAG fibres and the ease with which doped fibres were formed may result from different phase-transition kinetics for the pure and doped materials. In addition, the abrupt change in fibre-stinging behaviour at 1,600 K has characteristics of a phase transition from a smaller- to a much larger-viscosity liquid.

Glass-fibre synthesis should be possible for a wide range of oxide materials. We have also made glass fibres from alumina–silica compositions with Al_2O_3:SiO_2 up to 72:28, Mg_2SiO_4 (forsterite), $CaAl_2O_4$, $LaAlO_3$ and others. Although viscosity data for non-silicate oxides are lacking, it is apparent from glass-forming results that many, if not all, of these liquids are highly fragile. The method of containerless undercooling to access the higher viscosities required for glass-fibre-pulling should thus be applicable to the manufacture of fibres of a large number of new oxide compositions. □

1. Bass, M. (ed.) *Handbook of Optics* Vol. 2, *Devices, Measurements and Properties* 2nd edn (McGraw-Hill, New York, 1995).
2. Angell, C. A. in *Relaxations in Complex Systems* (eds Ngai, K. L. & Wright, G. B.) 3–11 (National Technical Information Service, US Dept of Commerce, Springfield, VA, 1985).
3. Angell, C. A. Formation of glasses from liquids and biopolymers. *Science* **267**, 1924–1935 (1995).
4. Debenedetti, P. G. *Metastable Liquids* (Princeton Univ. Press, 1997).
5. Fratello, V. J. & Brandle, C. D. Physical properties of a $Y_3Al_5O_{12}$ melt. *J. Cryst. Growth* **128**, 1006–1010 (1993).
6. Massiot, D., Taulelle, F. & Coutures, J. P. Structure diagnostic of high temperature liquid phases by ^{27}Al NMR. *Colloque Phys. C* **5**, 425–431 (1990).
7. Weber, J. K. R. & Nordine, P. C. Containerless liquid-phase processing at high temperatures. *Microgravity Sci. Technol.* **VII**, 279–282 (1995).
8. Weber, J. K. R., Felten, J. J. & Nordine, P. C. New method for high purity ceramic synthesis. *Rev. Sci. Instrum.* **67**, 522–524 (1996).
9. Loewenstein, K. L. *The Manufacturing Technology of Continuous Glass Fibres* (Elsevier, Amsterdam, 1973).
10. Laughlin, W. T. & Uhlmann, D. R. Viscous flow in simple organic liquids. *J. Phys. Chem.* **76**, 2317–2325 (1972).
11. Abell, J. S., Harris, I. R., Cockayne, B. & Lent, B. An Investigation of phase stability in the Y_2O_3-Al_2O_3 system. *J. Mater. Sci.* **9**, 527–537 (1974).
12. Caslavsky, J. L. & Viechnicki, D. J. Melting behavior and metastability of yttrium aluminum garnet (YAG) and $YAlO_3$ determined by optical differential thermal analysis. *J. Mater. Sci.* **15**, 1709–1718 (1980).
13. Aasland, S. & McMillan, P. F. Density-driven liquid-liquid phase separation in the system Al_2O_3-Y_2O_3. *Nature* **369**, 633–639 (1994).

C_{36}, a new carbon solid

C. Piskoti*†, J. Yarger‡† & A. Zettl*†

* *Department of Physics, University of California at Berkeley, 366 LeConte Hall, Berkeley, California 94720, USA*
† *Materials Sciences Division, Lawrence Berkeley National Laboratory, 1 Cyclotron Road, Berkeley, California 94720, USA*
‡ *Department of Chemistry, University of California at Berkeley, 420 Latimer Hall, Berkeley, California 94720, USA*

Under appropriate non-equilibrium growth conditions, carbon atoms form relatively stable hollow clusters of well-defined mass number[1], collectively known as fullerenes. The mass production, purification and condensation of such clusters into a molecular solid is generally essential to full experimental characterization: the initial discovery[2] of C_{60}, for example, had to await a bulk synthesis method[3] six years later before detailed characterization of the molecule was possible. Gas-phase experiments[1,4,5] have indicated the existence of a wide range of fullerene clusters, but beyond C_{60} only a few pure fullerene solids have been obtained[6], most notably C_{70}. Low-mass fullerenes are of particular interest because their high curvature and increased strain energy owing to adjacent pentagonal rings could lead to solids with unusual

intermolecular bonding and electronic properties. Here we report the synthesis of the solid form of C_{36} by the arc-discharge method[3]. We have developed purification methods that separate C_{36} from amorphous carbon and other fullerenes, to yield saturated solutions, thin films and polycrystalline powders of the pure solid form. Solid-state NMR measurements suggest that the molecule has D_{6h} symmetry, and electron-diffraction patterns are consistent with a tightly bound molecular solid with an intermolecular spacing of 6.68 Å. We observe large increases in the electrical conductivity of the solid on doping with alkali metals.

To determine the optimum parameters for C_{36} production, we performed a series of experiments in a helium-environment arc-discharge chamber originally designed for C_{60} production. An arc was started between two 1/4-inch-diameter graphite electrodes, using a d.c. current of 100 A while maintaining a 1-mm gap between electrodes. A removable metal substrate, designed for subsequent direct insertion into a mass spectrometer, was placed 10 cm from the discharge region on the wall of the water-cooled chamber. Arcing was maintained for several minutes until a uniform carbon film of approximate thickness 10 μm coated the substrate. A series of experimental runs was carried out at different fixed static helium pressures between 50 and 1,500 torr. Each of the substrates was then
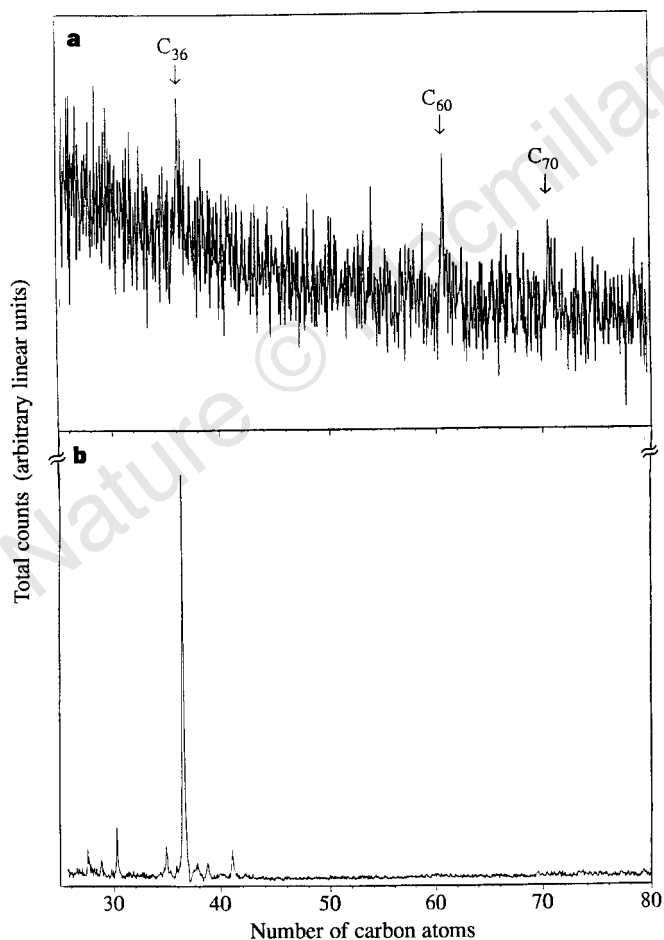

Figure 1 Mass spectra of films prepared in this study. **a**, Time-of-flight mass spectrum of a sample of crude fullerene soot produced at a helium pressure of 400 torr. The data show the presence of a peak at the mass of C_{36} (432 a.m.u.) with approximately the same intensity as the peak due to C_{60} (720 a.m.u.). **b**, Time-of-flight mass spectrum of material from a film evaporated from crude soot which had been depleted of C_{60} and C_{70} by toluene extraction. The peak at 438 a.m.u. is due to C_{36} which has been partially hydrogenated (six hydrogens per C_{36} molecule) during the high-temperature evaporation process.

loaded into a Micromass laser desorption/ionization time-of-flight mass spectrometer.

Figure 1a shows the mass spectrum of one of these films grown in 400 torr helium. The dominant peaks in the spectrum are at 720 and 432 atomic mass units (a.m.u.). The former peak corresponds to 60 carbon atoms, while the latter corresponds to 36 carbon atoms. The C_{60} and C_{36} peaks are of comparable magnitude and these molecular species appear to be the most prominent in the sample. Lesser peaks are also observed, for example at 840 a.m.u. (C_{70}). The synthesis of C_{36} is very sensitive to experimental conditions, notably the helium pressure: runs in this series at pressures significantly different from 400 torr failed to produce prominent peaks below 720 a.m.u. in the mass spectrum.

To produce bulk amounts of C_{36} suitable for purification, arcing runs in 400 torr helium were repeated and the resulting 'soot' was collected from the synthesis chamber walls. The soot was initially washed with toluene in a standard Soxhlet extractor which removed C_{60}, C_{70} and trace amounts of even higher-order fullerenes. Mass spectrometry on the toluene-soluble extract showed the expected fullerene peaks but no peak at 432 a.m.u., indicating that C_{36} is not soluble in toluene.

Two methods were subsequently used to separate C_{36} from the remaining toluene-insoluble material. In the first, sublimation-purification was used to produce thin films of C_{36}. Here the toluene-insoluble material was dried in vacuum at 150 °C for two hours and placed in the tungsten boat of a thermal evaporator. No precautionary steps were taken to protect the material from ambient moisture. The evaporator boat was heated under a pressure of less than 1 μtorr, ultimately reaching a temperature in excess of 1,500 °C. A metal substrate was suspended over the boat at a height of about 5 cm. In about 20 minutes, films of the order of 100 nm thick could be grown on the substrate. Notably, the black films were highly resistant to scratching, unlike amorphous carbon or C_{60} films.

Figure 1b shows the time-of-flight mass spectrum for the material of a thermally evaporated film. The film contains essentially a single molecular component of mass 438 a.m.u., 6 a.m.u. higher than the mass of C_{36}. Almost certainly the discrepancy is due to the partial hydrogenation of the C_{36} clusters through reaction with adsorbed moisture at the elevated temperature of evaporation. As expected, C_{36} is a fairly reactive material, more so than C_{60} or C_{70}.

To establish a purification method based on 'wet chemistry' rather than thermal evaporation, we tested sublimation-generated films prepared as above in a variety of organic solvents. The films were found to be insoluble in toluene and benzene, but soluble in pyridine and carbon disulphide (CS_2). However, unlike C_{60} and C_{70}, C_{36} is very slow to dissolve in either of these solvents and extensive heating and exposure to ultrasound are required to obtain a saturated solution. This is consistent with the strong, almost covalent bonding expected[7] between C_{36} molecules: C_{36} is not simply a van der Waals solid as is C_{60}.

The wet-chemistry purification method was used to produce bulk quantities of refined C_{36} powder. The crude arc-chamber soot was first Soxhlet-extracted with toluene to remove higher-order fullerenes, followed by Soxhlet extraction with pyridine. The pyridine-soluble extract forms a yellow-brown solution, as opposed to the toluene-soluble extract which is red-brown in colour. Overall, the crude soot was found to contain ~10% toluene-soluble material (C_{60} and C_{70}) and about 1–2% pyridine-soluble material (C_{36}). After evaporating the pyridine from the pyridine-soluble fraction, a black solid was obtained. This solid differs from that of the previously reported $C_{36}H_{12}$ bowl-shaped molecule in both colour and solubility[8].

To investigate the structure of the individual C_{36} molecules and the C_{36} molecular solid, we used solid-state ^{13}C NMR, bulk electron diffraction, mid-infrared transmission, and solid-state transport studies. It has been shown that for a 36-atom carbon cage with

hexagonal and pentagonal faces, 15 different isomers are possible[9]. Recent calculations indicate that of those isomers the lowest in energy are the structures with D_{6h} and D_{2d} symmetry[10]. These two molecules can be distinguished via NMR spectroscopy. The D_{6h} structure is expected to show three distinct ^{13}C NMR resonances of equal intensity, whereas the D_{2d} structure is expected to have five resonances, four with equal intensity and the fifth with half the intensity[9,11].

Figure 2 shows the experimental ^{13}C NMR spectrum for C_{36} powder, obtained using a Chemagnetics 500 MHz instrument with magic-angle spinning. The experimental spectrum contains two prominent peaks, one at 146.1 p.p.m. (relative to tetramethylsilane) and another (with approximately one-half the intensity) at 135.7 p.p.m. The inset to Fig. 2 shows the predicted molecular NMR spectra for the isolated D_{6h} and D_{2d} isomers (along with schematic structure drawings). The experimental spectrum appears inconsistent with predictions for the D_{2d} isomer. On the other hand, taking into account experimental broadening of the peaks, one would expect for the D_{6h} isomer two peaks, one near 135 p.p.m. and another 'double intensity' peak at higher p.p.m. arising from the two higher nearly degenerate resonances. This is precisely what is observed experimentally. The smaller experimentally observed shift of the 'double intensity' peak (at 146 p.p.m. versus the predicted 158 p.p.m.) is accounted for by additional shielding of these reactive carbon atom sites by neighbouring molecules in the solid (this shielding is not considered in the simple molecular calculations). We thus identify our C_{36} cage molecule as having D_{6h} symmetry.

To investigate the crystal structure of solid C_{36}, we performed electron diffraction experiments. A small amount of material obtained from the pyridine extraction was ground up, dispersed on a holey carbon grid, and inserted into a JEOL 200X transmission electron microscope (TEM). The material was observed to be polycrystalline with a crystallite grain size of ~100 nm. Using a field limiting aperture, the diffraction pattern of selected crystallites was recorded.

In Fig. 3 we show a TEM diffraction pattern for a C_{36} crystallite. The hexagonal diffraction pattern suggests a close-packing arrangement perpendicular to the zone axis. The pattern is reminiscent of diffraction patterns observed for C_{60} and C_{70}. However, the d-spacing measured from this pattern for the first-order diffracted spots is 6.68 Å, significantly less than the (100) d-spacing of 8.7 Å reported[3] for C_{60}. Unfortunately, because the C_{36} crystallites are platelets with high aspect ratios, this was the only zone axis along which the crystallites were thin enough to allow useful TEM imaging, and thus determination of the detailed C_{36} crystal structure was not possible. Using the C_{36} molecular diameter[7,10,11] of approximately 5 Å (carbon centre to carbon centre distance) and assuming that C_{36} crystallizes in close-packed planes, the diffraction results imply an intermolecular bond length of 1.7 Å, significantly smaller than the van der Waals distance of 3.4 Å in graphite. This is suggestive of strong crystal bonding.

Like higher-order fullerene solids, C_{36} appears to suffer some TEM-induced damage at an electron beam energy of 200 keV. Under continuous TEM observation, the sharp crystalline diffraction patterns were found to deteriorate for extended irradiation times. Additional studies were performed to investigate the long-term stability of solid C_{36} subject (only) to high ambient temperatures. C_{36} powder was heated in vacuum to 1,350 °C for 48 hours and then characterized by TEM imaging. Over 50% of the diffraction patterns obtained for the heat-treated material were graphitic, indicating that a large amount of the material had converted to the energetically more favourable graphite.

Specimens of solid C_{36} were further characterized by mid-infra-red transmission and d.c. electrical resistivity measurements. Figure 4 shows the room temperature mid-infrared transmission spectrum for C_{36} powder dispersed in KBr. Several prominent dips in the transmission are observed. In the simplest interpretation, these dips directly represent absorption bands for the C_{36} solid. The observed absorption resonances are in the fullerene range but, as expected, they do not precisely match those of previously known fullerenes. No additional absorption peaks for C_{36} were observed in the frequency range 2,000–5,000 cm^{-1}.
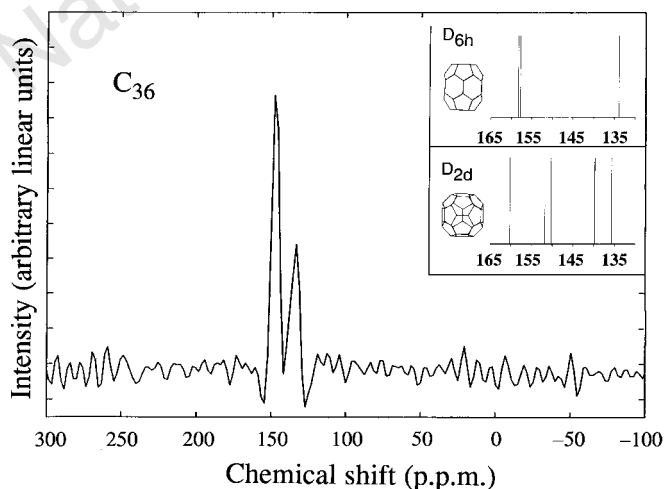
Figure 2 Predicted and observed NMR spectra of C_{36}. Main figure, ^{13}C NMR spectrum of C_{36} powder showing peaks at 146.1 and 137.5 p.p.m. with a 2:1 relative intensity ratio. Inset, the two lowest-energy isomers of the C_{36} molecule (with D_{2d} and D_{6h} symmetry) with the corresponding predicted NMR spectra[12]. Taking into account broadening and shielding for the solid, the experimental data suggest D_{6h} symmetry for the C_{36} molecule.

Figure 3 Electron-diffraction pattern of C_{36} crystallite. The pattern is hexagonal with a calculated d-spacing of 6.68 Å.
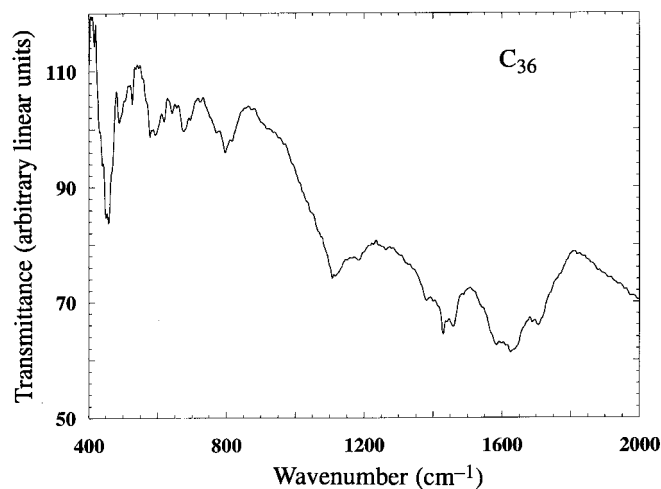
Figure 4 Infrared transmission spectrum of C_{36} powder in KBr.

For d.c. measurements, four-probe contacts were made to poly-crystalline specimens with conductive silver paint. At room temperature, the pure samples were insulating with a resistivity in excess of $10^7 \Omega$ cm. In fullerenes such as C_{60}, it is known that intercalation with alkali metals or alkaline earths drastically improves the electrical conductivity of the solid[1,12]. We have investigated this effect for C_{36}. Intercalation of the C_{36} solid with alkali metals was carried out using both sodium and potassium, by sealing the sample at one end of an evacuated tube with the alkali metal at the other end. The sample was then heated to ~250 °C while the metal was heated to ~175 °C. In both cases, the resistivity dropped by more than four orders of magnitude, to ~$10^3 \Omega$ cm at room temperature. The resistivity ρ as a function of temperature T for samples intercalated with either sodium or potassium was not metallic, but obeyed the functional form $\rho \sim \exp[T^{-\alpha}]$, behaviour typical of variable range hopping. At present it is not clear where in the structure, or how uniformly, the alkali metals intercalate.

If C_{36} could be made conducting with a sufficient density of states at the Fermi level—either by doping or by structural rearrangement (for example, induced by pressure)—one might expect, among other things, high-temperature superconductivity[10] with a transition temperature significantly exceeding that of intercalated C_{60}. These possibilities, along with details of the structure, electronic properties, and mechanical response of C_{36}, are at present being investigated. □

1. Billups, W. E. & Ciufolini, M. A. (eds) *Buckminsterfullerenes* (VCH, New York, 1993).
2. Kroto, H. W., Heath, J. R., O'Brien, S. C., Curl, R. F. & Smalley, R. E. C_{60}: buckminsterfullerene. *Nature* **318,** 162–163 (1985).
3. Kratschmer, W., Lamb, L. D., Fostiropoulos, K. & Huffman, D. R. Solid C_{60}: a new form of carbon. *Nature* **347,** 354–358 (1990).
4. Rohlfing, C. & Kaldor, J. Production and characterization of supersonic carbon cluster beams. *Chem. Phys.* **81,** 3322–3330 (1984).
5. O'Brien, S. C., Heath, J. R., Curl, R. F. & Smalley, R. E. Photophysics of buckminsterfullerene and other carbon cluster ions. *J. Chem. Phys.* **88,** 220–230 (1988).
6. Diederich, F. & Whetten, R. L. Beyond C_{60}: the higher fullerenes. *Acc. Chem. Res.* **25,** 119–126 (1992).
7. Côté, M., Grossman, J. C., Louie, S. G. & Cohen, M. L. Electronic and structural properties of molecular C_{36}. *Bull. Am. Phys. Soc.* **42,** 270 (1997).
8. Scott, L. T., Bratcher, M. S. & Hagen, S. Synthesis and characterization of a C_{36} subunit. *J. Am. Chem. Soc.* **118,** 8743–8744 (1996).
9. Fowler, P. W. & Manolopoulos, D. E. *An Atlas of Fullerenes* (Clarendon, Oxford, 1995).
10. Grossman, J. C., Côté, M., Louie, S. G. & Cohen, M. L. Prediction of superconductivity in solid C_{36}. *Bull. Am. Phys. Soc.* **42,** 1576 (1997).
11. Grossman, J. C., Côté, M., Louie, S. G. & Cohen, M. L. Electronic and structural properties of molecular C_{36}. *Chem. Phys. Lett.* **284,** 344–349 (1998).
12. Hebard, A. F. *et al.* Superconductivity at 18 K in potassium doped C_{60}. *Nature* **350,** 600–601 (1991).

Influence of iron availability on nutrient consumption ratio of diatoms in oceanic waters

Shigenobu Takeda

Biology Department, Central Research Institute of Electric Power Industry, Abiko, Chiba 270-11, Japan

The major nutrients (nitrate, phosphate and silicate) needed for phytoplankton growth are abundant in the surface waters of the subarctic Pacific, equatorial Pacific and Southern oceans, but this growth is limited by the availability of iron[1–5]. Under iron-deficient conditions, phytoplankton exhibit reduced uptake of nitrate[6] and lower cellular levels of carbon, nitrogen and phosphorus[7]. Here I describe seawater and culture experiments which show that iron limitation can also affect the ratio of consumed silicate to nitrate and phosphate. In iron-limited waters from all three of the aforementioned environments, addition of iron to phytoplankton assemblages in incubation bottles halved the silicate:nitrate and silicate:phosphate consumption ratios, in spite of the preferential growth of diatoms (silica-shelled phytoplankton). The nutrient consumption ratios of the phytoplankton assemblage from the Southern Ocean were similar to those of an iron-deficient laboratory culture of Antarctic diatoms, which exhibit increased cellular silicon or decreased cellular nitrogen and phosphorus in response to iron limitation. Iron limitation therefore increases the export of biogenic silicon, relative to nitrogen and phosphorus, from the surface to deeper waters. These findings suggest how the sedimentary records of carbon and silicon deposition in the glacial Southern Ocean[8] can be consistent with the idea that changes in productivity, and thus in drawdown of atmospheric CO_2, during the last glaciation were stimulated by changes in iron inputs from atmospheric dust.

Iron-enrichment bottle incubation experiments were performed with resident phytoplankton assemblages to determine the effect of iron on major-nutrient uptake in three upwelling areas of the open ocean where iron input from atmospheric dust is known to be low[9]; the Southern Ocean, the equatorial Pacific, and the subarctic North Pacific.

In the Southern Ocean, iron addition promoted chlorophyll *a* increase and nitrate decrease compared to the control, indicating iron limitation of phytoplankton growth and nutrient utilization (Fig. 1a, b). However, significant decrease of silicate was observed both in the iron-enriched bottle and in the control (Fig. 1c): the elemental ratio of nutrients consumed by the phytoplankton assemblage in the control bottle showed silicate:nitrate and silicate:phosphate ratios two times higher than that in the iron-enriched bottle (Table 1). Yet microscopic examinations showed substantial growth of large-size diatoms (*Chaetoceros* spp. and *Nitzschia* spp.) in the iron-enriched bottle. The phytoplankton assemblage in the control was composed mainly of the same species as in the iron-enriched bottle. Thus, the iron nutritional status of the diatoms appears to affect silicate utilization physiologically.

The iron-induced change in nutrient consumption ratio was also observed in a phytoplankton assemblage from the Southern Ocean incubated under low light intensity (Table 1). Low light tended to decrease the phytoplankton growth rate and nutrient utilization, while the chlorophyll *a* content per cell increased. Even under such light-limited conditions, iron enrichment halved the consumption ratio of silicate to nitrate and phosphate (Table 1). Thus, the iron nutritional status appears to affect the consumption ratio of major nutrients in the whole euphotic zone.

Essentially the same results were observed in waters taken from